

Room-Temperature Observation of the Zeeman Effect Through the Optical Pumping of Rubidium

University of Cambridge, HoC: Christoph Eigen

Experiment Completed: 30th January - 12th February 2025

Abstract

This experiment focuses on the phenomenon of optical pumping, which uses electromagnetic radiation to pump atoms to a set quantum state. This technique allows for the observation of Zeeman splitting at non-cryogenic temperatures. Rubidium atoms were optically pumped with σ^+ light, and transitions were induced using perpendicular DC and RF magnetic fields. Using the low-field Zeeman resonance peaks, the Landé g-factors were measured to be $g_F(^{87}\text{Rb}) = 0.503 \pm 0.002$ and $g_F(^{85}\text{Rb}) = 0.345 \pm 0.003$, deviating slightly from theoretical values. The Earth's magnetic field was found to be $B_{\text{Earth}} = 0.291 \pm 0.002$ Gauss. Investigating the transient effects allowed for a measurement of the ratio of the Landé g-factors, 1.49 ± 0.06 , which was within error of the theoretical prediction. An investigation into power broadening revealed saturation at $V_{\text{RF}} = 11\text{V}$. The effects of a high magnetic field were analysed, but the experiment was limited by the strength of the coils in the setup. Multi-photon transitions were successfully observed; however, an unexpected resonance was found at 0.068 Gauss, suggesting the presence of systematic errors or off-resonant transitions. The results demonstrate the technique of optical pumping, but further experimentation is required for investigation into higher magnetic fields and to find the origin of the unexplained resonance.

Contents

1	Introduction	3
2	Theory	3
2.1	Rubidium, Hyperfine Structure and the Zeeman Effect	3
2.2	Optical Pumping	4
3	Low Field Resonances	5
3.1	Zero Field Transition	5
3.2	Zeeman Resonances	5
3.3	Discussion	5
4	Field Calibrations	6
5	Transient Effects	7
5.1	Theory	7
5.2	Method, Results, and Discussion	7
6	Lineshape Broadening	9
6.1	Theory	9
6.2	Method, Results, and Discussion	10
7	High Magnetic Field Transitions	10
7.1	Theory	10
7.2	Method, Results, and Discussion	11
8	Multi-photon Transitions	11
8.1	Theory	11
8.2	Method, Results, and Discussion	12
9	Conclusion	13
A	Appendix	15
A.1	Spectral Analysis of Signal Generator	15

1 Introduction

Developed by Nobel Prize winner Alfred Kastler in 1966 [1], optical pumping uses electromagnetic radiation to *pump* atoms to a specific quantum state. It is widely used in lasers to achieve population inversion [2]. Alkali metals are often used for analysing optical pumping phenomena due to their hydrogen-like properties. Rubidium is used in this experiment.

This report begins by explaining the relevant theory in Section 2. The low-field Zeeman resonances are explored in Section 3, followed by the necessary field calibrations in Section 4. Transient phenomena is explored in Section 5. In Section 6 the effects of line-shape broadening are investigated. Finally, sections 7 and 8 briefly investigate the effects of higher magnetic fields and multi-photon transitions, respectively.

2 Theory

2.1 Rubidium, Hyperfine Structure and the Zeeman Effect

Rubidium is an alkali metal of two major isotopes, ^{85}Rb (72%) and ^{87}Rb (28%) [3]. In this experiment, the focus is on its single valence electron. This outer electron is described by its spin (\mathbf{S}), orbital (\mathbf{L}), and total ($\mathbf{J} = \mathbf{L} + \mathbf{S}$) angular momentum. Coupling between \mathbf{L} and \mathbf{S} results in *fine splitting*, separating the $^2\text{P}_{1/2}$ and $^2\text{P}_{3/2}$ states. The nucleus contributes angular momentum \mathbf{I} , giving total angular momentum $\mathbf{F} = \mathbf{J} + \mathbf{I}$. Coupling between \mathbf{J} and \mathbf{I} causes *hyperfine splitting* of the individual P states.

The total atomic magnetic moment is the sum of the electronic and nuclear moments. The hamiltonian for the interaction with an external magnetic field \mathbf{B} is given by $H = g_J(\mu_B + \mu_N)\mathbf{J} \cdot \mathbf{B} \simeq g_J\mu_B\mathbf{J} \cdot \mathbf{B}$. The nuclear magnetic moment is neglected since $\mu_B \gg \mu_N = \frac{\mu_B}{1836}$.

Under a weak magnetic field, \mathbf{F} precesses about \mathbf{B} at the *Larmor frequency*, which is the Zeeman Effect. The effective hamiltonian becomes: $H = g_F\mu_B\mathbf{F} \cdot \mathbf{B}$ where g_F arises from the projection of \mathbf{J} onto \mathbf{F} [4]. The interaction energy is $W = g_F\mu_B B m_F$, where m_F is the component of the electron spin along \mathbf{B} . The energy gap for a $\Delta m_f = +1$ transition is $\Delta E = W(m_F + 1) - W(m_F) = g_F\mu_B B(m_F + 1 - m_F) = g_F\mu_B B$, since $\Delta E = h\nu$ the frequency required to cause such a transition is:

$$\nu = g_F\mu_B \frac{B}{h} \quad (1)$$

The magnetic field splits each of the hyperfine levels into $2\mathbf{F}+1$ sublevels ($m_F = -F, -F+1, \dots, F-1, F$), these sublevels follow the *Breit-Rabi formula*:

$$W = -\frac{\Delta W}{2(2I+1)} - \frac{\mu_N}{I} B m_F \pm \frac{\Delta W}{2} \sqrt{1 + \frac{4m_F}{2I+1}x + x^2} \quad (2)$$

Where $x = (g_J - g_I)\frac{\mu_B B}{\Delta W}$, $g_I = -\frac{\mu_N}{I\mu_B}$, W is the interaction energy, and ΔW is the hyperfine energy splitting. A detailed derivation can be found in Woodgate (1980) [5]. A plot of the Breit-Rabi equation is shown in figure 1 for $F = 2$ and $I = \frac{3}{2}$.

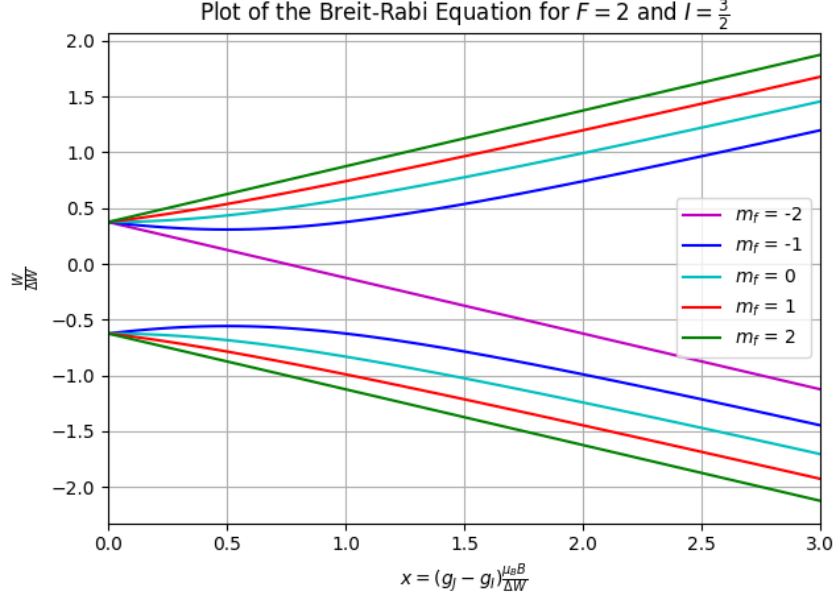


Figure 1: Plot of the Breit-Rabi equation for $F = 2$ and $I = \frac{3}{2}$. The hyperfine sublevels split under a magnetic field and are quadratic in the region $0.1 \lesssim x \lesssim 1.5$ before becoming linear.

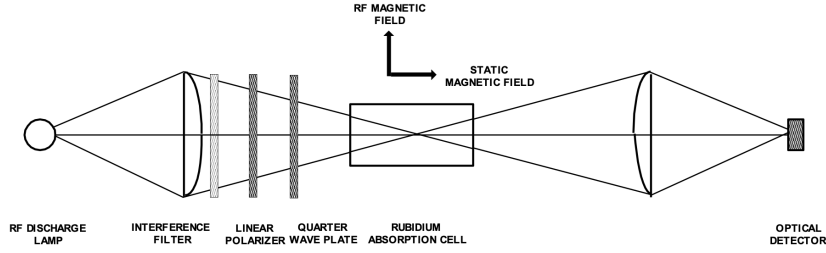


Figure 2: Apparatus used for Optical Pumping.

2.2 Optical Pumping

If an incoming beam of light is resonant with a Zeeman transition, it is absorbed by atoms, which become excited. The excited atom decays, emitting light in all directions, with a negligible amount transmitted to the outgoing beam. This experiment focuses on circularly polarised light resonant with transitions from the $^2S_{1/2}$ state to P states. σ^+ circularly polarised light carries spin angular momentum of $+\hbar$ [6] restricting transitions to $\Delta m_F = +1$ to conserve momentum.

An RF discharge lamp containing xenon and enriched rubidium ($^{87}\text{Rb} = 64\%$, $^{85}\text{Rb} = 36\%$) produces resonant light. The gas is ionised by the high electric field in the lamp, causing electron collisions that excite rubidium atoms, producing the emission spectrum of rubidium. Two main lines ($D_1 = 795\text{ nm}$ and $D_2 = 780\text{ nm}$) are emitted with the D_2 line removed by an interference filter. The remaining light is σ^+ polarised and passes through the rubidium-containing absorption cell, heated to 50°C to generate vapour. A buffer gas minimises cell wall collisions. A DC magnetic field is applied along the optical axis, while a transverse RF field induces Zeeman transitions.

The transitions that are of interest in this experiment are magnetic dipole transitions within the hyperfine structure and between the magnetic sublevels. Which transitions occur depends on the orientation of the RF field with respect to the DC field. In this

experiment, the RF is perpendicular to the DC field, meaning the only observable transitions are $\Delta F = 0$ and $\Delta m_F = \pm 1$.

Optical pumping drives atoms away from equilibrium by the resonant light absorption. Since only $\Delta m_F = +1$ are allowed, electrons are pumped into the $m_F = +2$ state for ^{87}Rb since there is no $m_F = 3$ state. Excited states can decay back into this level by spontaneous emissions, providing a path in but not out of the state. The same is true for ^{85}Rb except the pumped state is $m_F = +3$. The state population is monitored by the transmitted light intensity, which is measured by a 100 k Ω photodiode.

An RF frequency was provided by a 20 V signal generator, with spectral analysis confirming minimal harmonics (see Appendix A.1). The photodiode output and magnetic field currents were all measured using a PicoScope series 2000.

3 Low Field Resonances

In this experiment, the Zeeman resonances and zero field transition are measured for various RF frequencies. The sweep field coils are in a Helmholtz configuration, meaning the B field can be determined from the current in the coils using equation 3.

$$B = \left(\frac{4}{5}\right)^{\frac{3}{2}} \frac{\mu_0 N I}{R} \quad (3)$$

3.1 Zero Field Transition

The interaction between an atom and a magnetic field splits the hyperfine sublevels. If there is zero field, these levels are degenerate, a population imbalance is not established, and more light is absorbed (see the central dip in figure 3). The absorption dip at zero field allows an indirect measurement of the Earth's field. The sweep field current required for the dip was constant for different RF frequencies, as expected for the zero field transition. The dip occurred at an average current of 0.482 ± 0.004 A corresponding to a field (using equation 3) of 0.291 ± 0.002 Gauss (10^{-4}T).

Initially, the zero-field transition peak is broad and unresolved. The apparatus must be calibrated according to the local field in the room. Optimal alignment of the apparatus was in the east-west direction (with RF probing in north-south), and a vertical field was applied until minimum linewidth was achieved. This calibration is necessary to resolve Zeeman peaks (Figure 3).

3.2 Zeeman Resonances

The other peaks shown in Figure 3 are due to Zeeman resonances. Figure 4 shows how the frequency varies with the field. The field values are corrected by subtracting the zero field transition current. Using equations 3 and 1, the experimental Landé g-factors are 0.503 ± 0.002 for ^{87}Rb and 0.345 ± 0.003 for ^{85}Rb . These values differ from the theoretical values ($g_F = \frac{1}{2}$ for ^{87}Rb and $g_F = \frac{1}{3}$ for ^{85}Rb) by 0.6% and 3.5% respectively.

3.3 Discussion

Various factors affect the height of the ^{87}Rb and ^{85}Rb peaks. ^{85}Rb is more abundant, increasing absorption, and it's higher spin of $I_{^{85}\text{Rb}} = 5/2$ (vs. $I_{^{87}\text{Rb}} = 3/2$) allows for

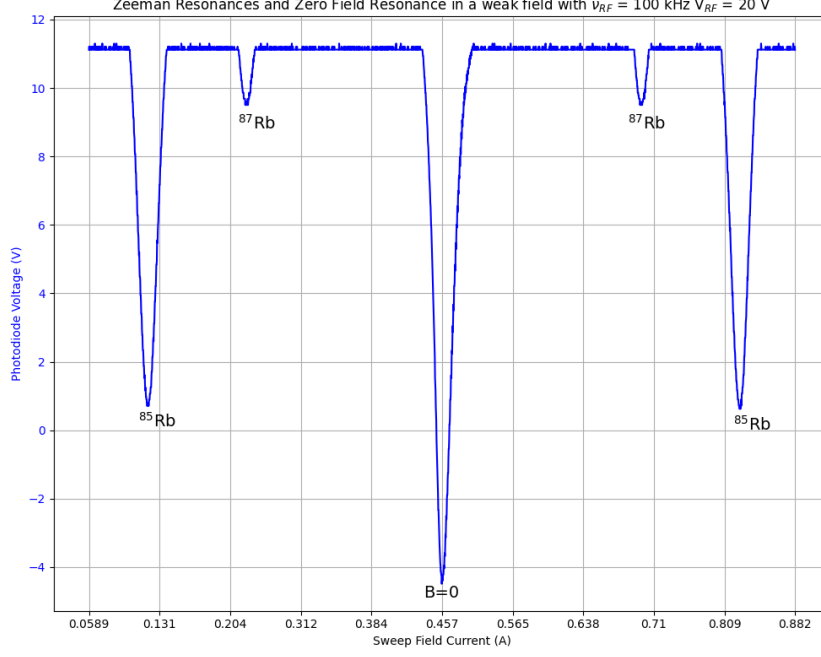


Figure 3: Plot showing the Zeeman resonances and zero field resonance in the low field regime. Appropriate peaks are labelled. The position of the zero-field peak gives a measurement of the Earth's magnetic field of 0.291 ± 0.002 Gauss.

more Zeeman transitions, increasing probability of absorption.

Figure 4 shows that the magnetic field at which the resonances occur is directly proportional to the RF frequency, in agreement with equation 1. ^{85}Rb transitions occur at higher fields since it has a lower value of g_F . The measured g_F for ^{85}Rb varies more from theory than g_F for ^{87}Rb . This could be due to increased broadening for ^{85}Rb since it has more available transitions or calibration errors, which would be higher for the higher field ^{85}Rb peak.

The errors in field current are significant; repeating measurements would be recommended to increase accuracy. The values of current were obtained manually in Picoscope; it would be more accurate to obtain them via fitting with a Gaussian/Lorentzian peak in Python.

4 Field Calibrations

Using theoretical values of g_F , Equation 1 gives the B field required for a certain RF frequency. Combining this with the coil current required experimentally, a relationship between coil current and the field can be found (Figure 5a). The Earth's field can be found from the intercept, where the field is zero. The Earth's field is determined to be 0.300 ± 0.009 gauss. This value and the value calculated in Section 3.1 do not lie within error of each other.

The value calculated here assumes theoretical g_F values, thereby assuming perfect calibration, which is not necessarily the case. A weighted mean of the two values gives $B_{\text{Earth}} = 0.291(4) \pm 0.001(9)$, matching the value in Section 3.1. This value is likely a more accurate measure for B_{Earth} . The larger main field coils are calibrated similarly with the result shown in figure 5b,

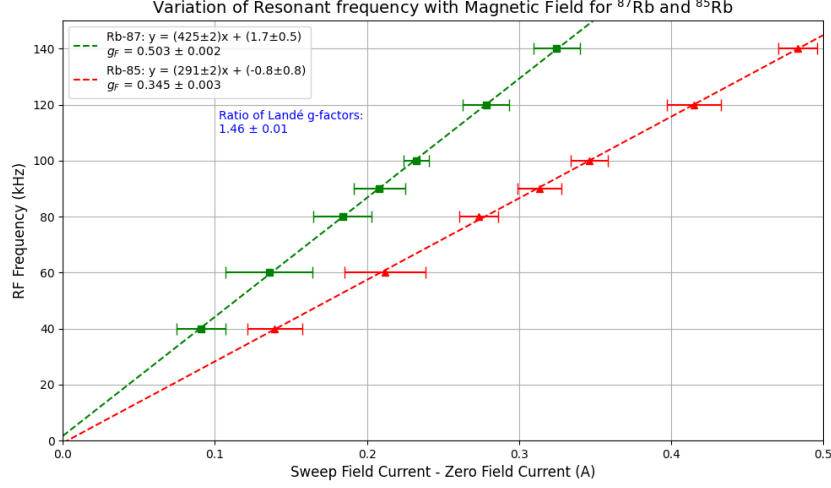
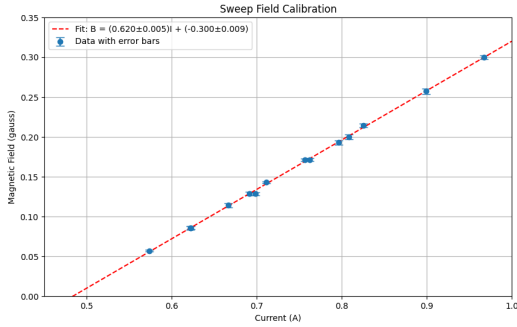
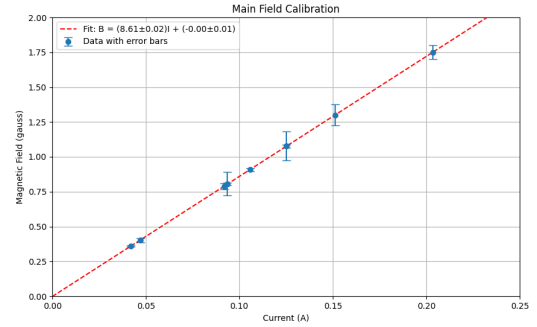


Figure 4: Plot showing the variation of the RF frequency of Zeeman transitions with the sweep field current. The Landé g -factors are determined from the gradients of the line and are 0.503 ± 0.002 for ^{87}Rb (green line) and 0.345 ± 0.003 for ^{85}Rb (red line). The ratio of these factors is 1.46 ± 0.01 .



(a) Sweep Field Calibration.



(b) Main Field Calibration.

Figure 5: Plots showing the calibration curves for the main and sweep fields, which are used to more accurately determine the field strength from the field current.

5 Transient Effects

5.1 Theory

In a two-level system ($m_F = +1, +2$), optical pumping creates an excess population in $m_F = +2$. If RF is applied at the resonance frequency, the populations of the two levels are equalised.

If the RF is suddenly applied at resonance after optical pumping equilibrium has been obtained, the excess population in the upper state decays to the lower state, causing a drop in transmitted light intensity. As the lower state is now overpopulated, the process reverses, creating a *ringing* oscillation in the transmitted light [7].

5.2 Method, Results, and Discussion

Transient effects were analysed by gating the RF at 50 Hz. An RF frequency of 100 kHz was used.

Figure 6a shows the photodiode output when the RF is switched off and pumping

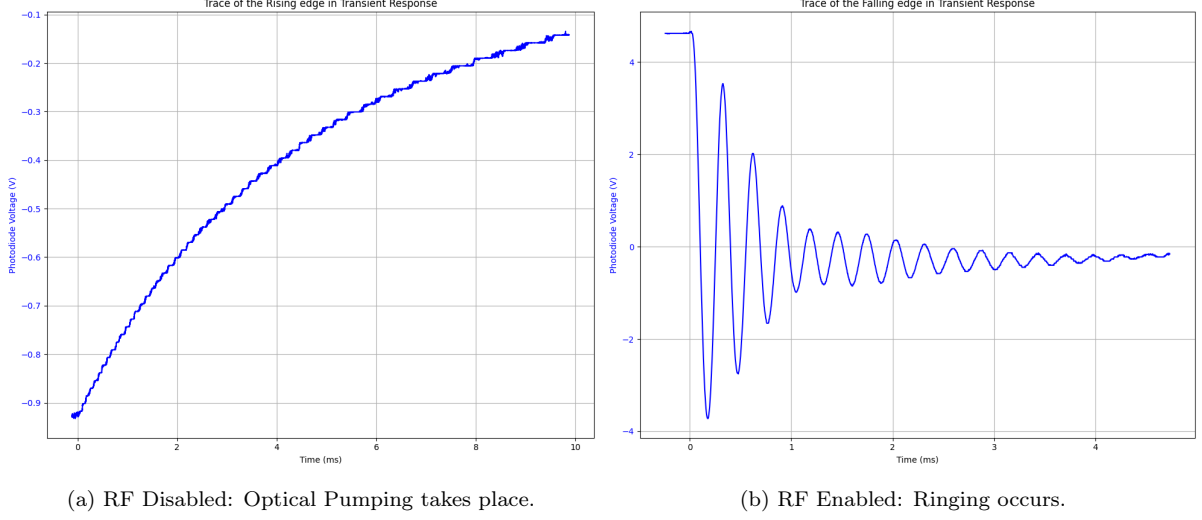


Figure 6: Traces of the transmitted light intensity in transient phenomena.

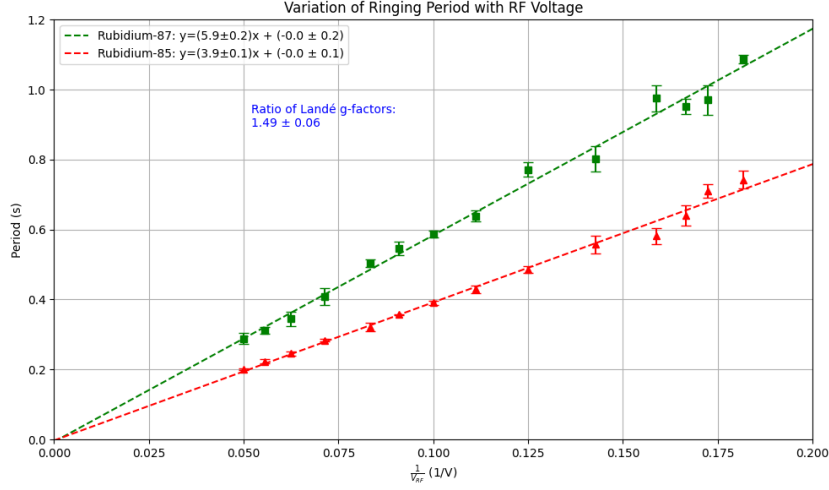


Figure 7: Plot showing the relationship between the ringing period and the RF voltage (green line for ^{87}Rb and red line for ^{85}Rb). An inverse relationship is demonstrated. The ratio of the gradients (1.49 ± 0.06) gives the ratio of the Landé g -factors.

occurs. The time constant of the pumping was $\tau = 1.64 \pm 0.08$ ms. Figure 6b shows the ringing signal when the RF is turned on; the time constant for the decay was $\tau = 3.30 \pm 0.09$ ms. Both time constants stayed constant with varying V_{RF} . The decay constant is expected to be constant with voltage as the decay is thermal, which is usually $\propto k_{\text{B}}T$ rather than V_{RF} . The period of ringing oscillations (measured using built-in PicoScope analysis) did vary with the V_{RF} , with an inverse relationship (Figure 7).

This is expected since the period corresponds to a precession of \mathbf{F} about the RF field [8]. The ratio of the gradients in figure 7 gives the ratio of the Landé g -factors [8] for ^{87}Rb and ^{85}Rb and is found to be 1.49 ± 0.06 , which is within error of the theoretical prediction of 1.5.

This experiment proved difficult to complete due to the prevalence of 50 Hz main noise. Efforts were made to reduce this by sampling at 50 Hz as well as implementing a digital high-pass filter. The data still proved difficult to take; the measurements were taken four times to increase the accuracy of the results.

6 Lineshape Broadening

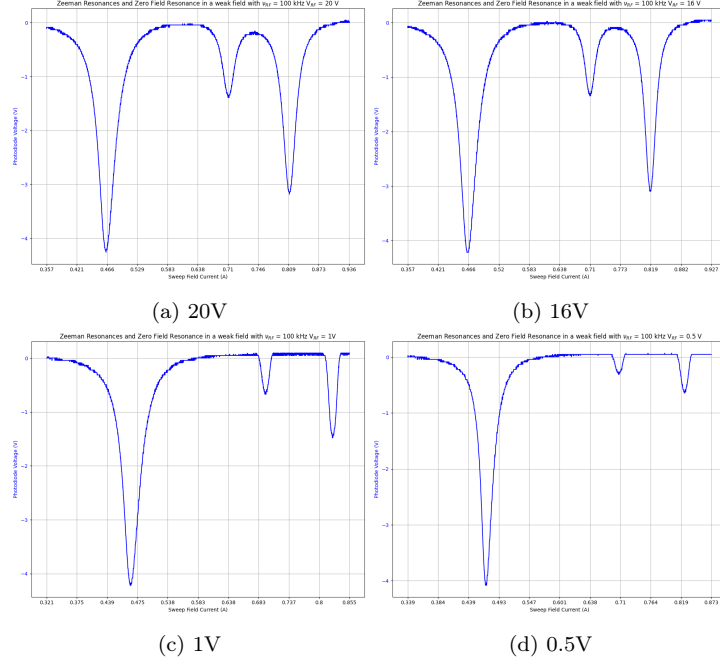


Figure 8: Traces of the Low Field Zeeman resonances of ^{87}Rb and ^{85}Rb for voltages of 0.5, 1.0, 16, and 20V. At low voltages, no broadening occurs, but the peak height increases with voltage. At higher voltages, there is saturation, the peak height stays constant, and the lineshape broadens.

6.1 Theory

Different types of spectral linewidth broadening occur in this experiment. Doppler broadening occurs due to the difference in frequency of radiation in the laboratory frame and in the frame of an atom moving at speed v . This causes the absorption dip to take a Gaussian form rather than Lorentzian [9].

$$\omega' = \omega - kv \quad (4)$$

The change in frequency is given by equation 4, where $k = \frac{2\pi}{\lambda}$. Calculating v using $\frac{1}{2}mv^2 = k_B T$ and using $f = 100$ kHz, we find that $\Delta f \simeq 100$ mHz. The FWHM in this experiment are on the order of 10 Hz so Doppler broadening can be expected to have a small effect.

At high intensities of radiation, the spectral linewidth of an absorption is observed to increase with the intensity, an effect known as *power broadening* [10]. It can be shown that at high intensities the FWHM obeys equation 5, where $I_{\text{sat}} = \frac{\pi}{3} \frac{hc}{\lambda^3 \tau}$ is the saturation intensity [4], which is the intensity at which the transition achieves maximum population difference [4]. Note that $I \propto |A|^2 \propto V^2$.

$$\Delta\omega_{\text{FWHM}} = \Gamma \left(1 + \frac{I}{I_{\text{sat}}} \right)^{\frac{1}{2}} \quad (5)$$

The presence of nearby particles also affects the linewidth of the absorption; this effect is known as *pressure broadening*. This occurs when the light-emitting rubidium particles collide with the buffer gas particles, smearing out the energy levels of the rubidium.

6.2 Method, Results, and Discussion

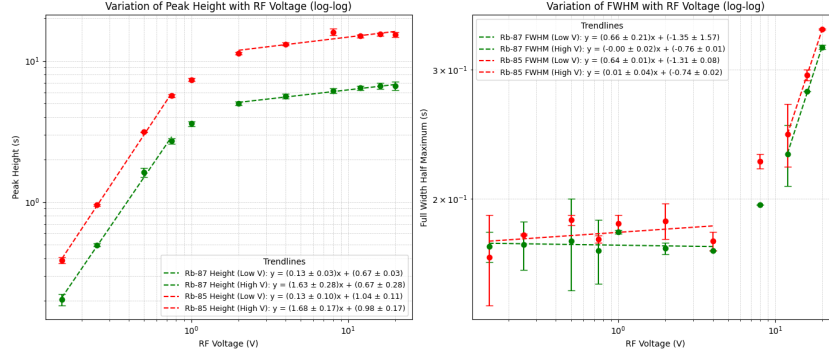


Figure 9: Plot showing the voltage dependencies of the peak height and FWHM (green line for ^{87}Rb and red line for ^{85}Rb). At low voltages, the peak height increases and FWHM stays constant. At higher voltages (above saturation), the peak height is constant and FWHM increases.

The effect of the RF voltage on the peak height and full width half maximum is shown in Figure 9. Both plots show two regimes. The peak height is constant at high voltage, whereas at low voltages this increases according to $V^{1.63 \pm 0.28}$ for ^{87}Rb and $V^{1.68 \pm 0.17}$ for ^{85}Rb . The opposite is true for the full width half maximum; it remains constant for low voltages, then increases at high voltages where power saturates, following $V^{0.66 \pm 0.21}$ for ^{87}Rb and $V^{0.64 \pm 0.01}$ for ^{85}Rb .

Peak height should increase with power ($\propto V^2$) at low voltages before saturation since the increased power increases the rate of transitions. Figure 9 gives the relationship as $V^{1.67 \pm 0.14}^\dagger$ which is not within error of V^2 . A linear regime is then seen where saturation occurs as expected.

The FWHM remains constant until around 13 V after which it increases linearly with $V^{0.660.21}$. Equation 5 states the FWHM is $\propto \sqrt{I_{\text{sat}}} \propto V$. Figure 9 gives the relationship as $V^{0.64(4)0.00(9)}$ which lies in between \sqrt{V} and V . This suggests the presence of additional power-related broadening.

In summary, at low power, we see a linear increase in the peak height with $\sim V^{\frac{5}{3}}$ until it saturates at approximately $V = 11$ V, after which the peak height no longer increases and instead the FWHM starts to increase with $\sim V^{\frac{2}{3}}$. The difference between this and the expected relationship implies additional broadening effects.

These results are also illustrated in Figure 8. Figures 8a and 8b show that at high voltage peak height is constant but FWHM increases, while Figures 8c and 8d show that at low voltages the FWHM is constant but the height increases.

7 High Magnetic Field Transitions

7.1 Theory

The resonances are now studied at much higher magnetic fields in order to observe the quadratic region seen in figure 1 ($0.1 \lesssim x \lesssim 1.5$). The energy levels split into $2F + 1$

[†]This was calculated using an error-weighted mean of the relationships for ^{87}Rb and ^{85}Rb since it is expected the two isotopes follow the same relationship. The same calculation was done for the FWHM relationship below.

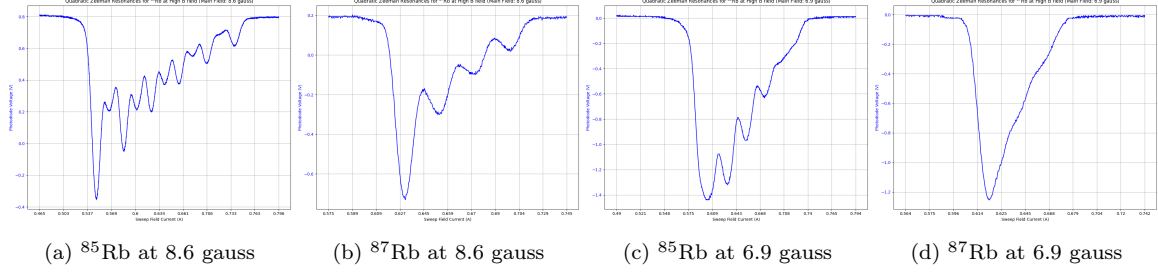


Figure 10: Traces of the quadratic Zeeman resonances of ^{87}Rb and ^{85}Rb for main fields of 8.6 and 6.9 Gauss. At 8.6 Gauss, ^{85}Rb peaks are resolvable, whilst ^{87}Rb peaks are only partially resolvable. At 6.9 Gauss resolution is poor.

sublevels under the field, but now with unequal spacing, meaning there are now $2F$ possible resonances. For ^{87}Rb , $F = 2$ and we expect to see 6 resonances (4 $F = 2$ and 2 $F = 1$ transitions). $F = 1$ amplitudes are much smaller since the energy gap is smaller as the states are closer together. For ^{85}Rb , $F = 3$ and we see 10 resonances (6 $F = 3$ and 4 $F = 2$ transitions). Again, the amplitudes for $F = 2$ are smaller due to a lower energy gap.

7.2 Method, Results, and Discussion

The high B field is created using powerful Helmholtz coils (main field coils) oriented along the direction of the sweep field. The sweep coils are used in the usual way, except now they are sweeping at a much higher field. The results are displayed in figure 10. The overall field is determined by adding the sweep field (from figure 5b) to the main field.

At a field of 6.9 Gauss (Figures 10c and 10d) some peaks overlap and cannot be resolved. The highest field that the main field coils can achieve was found to be at a coil current of 1A corresponding to a field of 8.6 Gauss; the results are seen in figures 10a and 10b. ^{85}Rb (Figure 10a) shows 10 peaks; the $F = 3$ transitions correspond to the six larger ones. The smaller peaks may correspond to $F = 2$ transitions or double quantum transitions, which are predicted to have similar absorption levels [8]. ^{87}Rb (Figure 10a) shows only 4 peaks, corresponding to $F = 2$ transitions; the $F = 1$ peaks are not seen. The smaller $F = 1$ peaks are blended with the larger $F = 2$ peaks and cannot be resolved.

This experiment is limited by the strength of the main field coils, causing peaks to overlap, meaning peak positions cannot be accurately determined. The peaks also suffer from lineshape broadening (see Section 6) since the experiment is conducted at $V_{\text{RF}} = 20\text{V}$, which was necessary to achieve better peak resolution. This would lead to wider peaks, which leads to more peak overlapping. This experiment should be repeated at a higher magnetic field and a lower voltage to improve results.

8 Multi-photon Transitions

8.1 Theory

In addition to single-photon transitions, transitions can occur when an atom simultaneously absorbs two (or more) photons. Multi-photon transitions are made possible by the relaxation of parity selection rules (see Bonin et al. (1984) [11]) and the presence of virtual states. These virtual states are not eigenfunctions of any operator and are not

observable [12]. The existence of the virtual state is governed by $\Delta E \Delta t = \frac{\hbar}{2}$. Upon absorption of a photon, the atom can then either absorb a further photon to complete the transition or decay back to the original state. Multi-photon transitions can either be degenerate (same frequency) or non-degenerate (different frequency). Assuming degenerate absorption, Equation 1 generalises to equation 6 where N is the number of photons in the transition. [13]

$$\nu = g_F \mu_B \frac{B}{N \hbar} \quad (6)$$

8.2 Method, Results, and Discussion

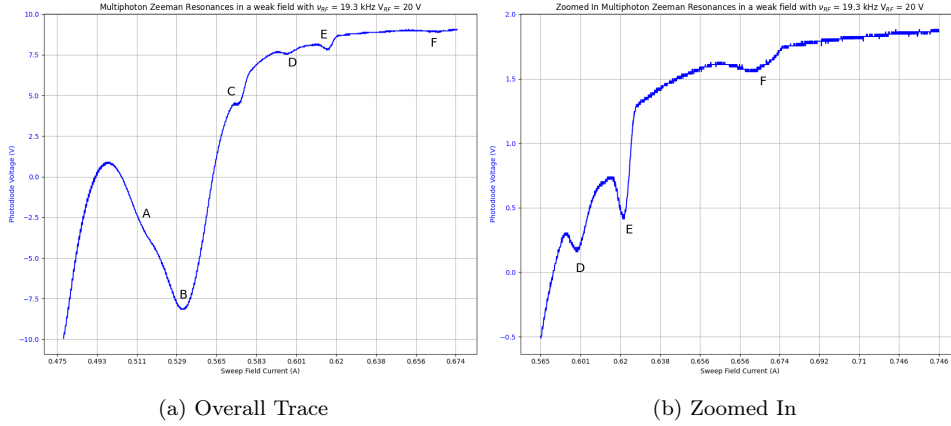


Figure 11: Multiphoton Trace showing the resonances for multi-photon transitions. Peaks A and B are single-photon transitions; C is a double-photon transition. Peak E represents both the double photon transition for ^{85}Rb and the triple photon for ^{87}Rb ; hence, it has a large amplitude. Peak F corresponds to the triple photon absorption for ^{85}Rb . Peak D cannot be identified.

The Rubidium was probed at a voltage of $V_{RF} = 20$ V and an RF frequency of 19.3 kHz, the lowest frequency that yielded the maximum number of resolvable peaks. The results are displayed in Figure 11, Figure 11a displays the trace starting at the zero field resonance, and Figure 11b is a zoomed-in version of the second half of the graph. The theoretical sweep field at which multiphoton transitions occur at $\nu = 19.3$ kHz can be determined using Equation 6. This can then be turned into a sweep field current using Figure 5a and can be compared to the values measured in the traces in Figure 11. The results of this are shown in Table 1. Peaks A and B are single-photon transitions; C is a double-photon transition. Peak E represents both the double photon transition for ^{85}Rb and the triple photon for ^{87}Rb ; hence, it has a large amplitude. Peak F corresponds to the triple photon absorption for ^{85}Rb . The multi-photon peaks are expected to vary quadratically with intensity [14]. This could be tested by taking more readings at different RF voltages.

Peak D, at 0.068 Gauss, cannot be matched with any multiphoton transitions. A potential source of this peak could be from a non-degenerate multi-photon transition or another off-resonant transition. It could also be due to magnetic inhomogeneities or hysteresis effects; these could be ruled out by reversing the field and checking if the peaks remain at the same fields. If hysteresis is present, the results can be shifted to eliminate it. If after this Peak D is still present, it is likely due to another transition.

Isotope	N_γ	$B_{\text{theoretical}}/\text{Gauss}$	$I_{\text{theoretical}}/\text{A}$	$I_{\text{observed}}/\text{A}$	Peak	%Error
^{87}Rb	1	0.0276	0.528	0.52 ± 0.01	A	1.6%
^{85}Rb	1	0.0414	0.550	0.55 ± 0.02	B	1.0%
^{87}Rb	2	0.0552	0.573	0.57 ± 0.01	C	0.12%
^{85}Rb	2	0.0828	0.618	0.62 ± 0.02	E	0.53%
^{87}Rb	3	0.0828	0.618	0.62 ± 0.02	E	0.53%
^{85}Rb	3	0.124	0.684	0.68 ± 0.03	F	1.1%

Table 1: Comparison of multiphoton predicted sweep currents with experimental currents for $\nu_{\text{RF}} = 19.3 \text{ kHz}$ and $V_{\text{RF}} = 20 \text{ V}$.

9 Conclusion

This experiment investigated optical pumping, which enables the observation of the quantum Zeeman effect at close to room temperature, allowing for the studying of quantum effects without the need for cryogenic temperatures.

The low-field resonances were used to measure the Landé g-factors as $g_F = 0.503 \pm 0.002$, and $g_F = 0.345 \pm 0.003$ for ^{87}Rb and ^{85}Rb , deviating from ($\frac{1}{2}$ and $\frac{1}{3}$) theoretical values by 0.6% and 3.5% respectively. The larger error for ^{85}Rb could be due to increased broadening or calibration errors at the higher field. Accuracy could be improved by using curve fitting in Python instead of manually taking measurements in Picoscope.

Measurement of the zero field transition along with a calibration of the sweep field allowed for a measurement of the Earth's magnetic field, $B_{\text{Earth}} = 0.291 \pm 0.002 \text{ Gauss}$.

The transient effects allowed for a further determination of the Landé g-factors, in the form of their ratio, to be 1.49 ± 0.06 , consistent with the theoretical prediction of 1.5.

The effect of RF power on linewidth broadening was analysed, and saturation was seen above $\sim 11\text{V}$, after which the signal began to broaden. The relationship of the FWHM with voltage indicated that the broadening was not just down to power broadening and that other phenomena may be involved.

Finally, resonances at high fields and multi-photon transitions were investigated. The expected transitions were seen for ^{85}Rb at high field, but poor resolution of peaks meant not all predicted ^{87}Rb were observed. More powerful coils would be required for complete resolution of the peaks. The investigation into multiphoton transitions showed 2 and 3 photon transitions for both isotopes; however, an unidentifiable peak was observed. This peak could be due to hysteresis effects from an inhomogeneous magnetic field, which could be tested by reversing the sweep field, or it could be due to another non-resonant or non-degenerate transition. Further investigation is warranted to determine the origin of the peak.

[Word Count: 2940]

References

- [1] A. Kastler. Optical methods for studying hertzian resonances. *Science*, 158, 1967.
- [2] Walter Koechner. Solid-state laser engineering. 1992.
- [3] Commission on Isotopic Abundances and Atomic Weights. *Standard Atomic Weights: Rubidium*. 1969.
- [4] Christopher J. Foot. *Atomic Physics*. 2013.
- [5] Gordon Kemble Woodgate. *Elementary Atomic Structure*. Oxford University Press, 2nd edition, 1980. p. 193-194.
- [6] L. Yang, F. Khosravi, and Z. Jacob. Quantum field theory for spin operator of the photon. 2020.
- [7] Michel Le Bellac. *A Short Introduction to Quantum Information and Quantum Computation*. 2006.
- [8] TeachSpin. *Optical Pumping Of Rubidium OP1-B, Guide to the Experiment*. 2002.
- [9] A. E. Siegman. *Lasers*. 1986. p. 1184.
- [10] N.V. Vitanov, B.W. Shore, L. Yatsenko, K. Böhmer, T. Halfmann, T. Rickes, and K. Bergmann. Power broadening revisited: theory and experiment. *Optics Communications*, 199(1):117–126, 2001.
- [11] Keith D. Bonin and Thomas J. McIlrath. Two-photon electric dipole selection rules. *JOSA B*, 1984.
- [12] B.R Masters. Historical development of non-linear optical microscopy and spectroscopy. *Handbook of Biomedical Nonlinear Optical Microscopy*, 2008. p. 10.
- [13] William Happer. Optical pumping. *Reviews of modern physics*, 1972.
- [14] Nikolai V. Tkachenko. Two photon absorption. 2006.

A Appendix

A.1 Spectral Analysis of Signal Generator

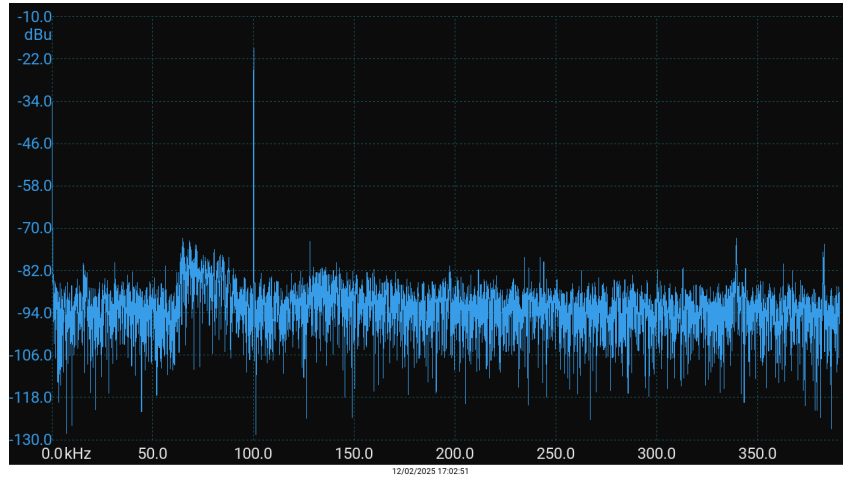


Figure 12: Spectral view of the output of the 20 V signal generator at a voltage of 250 mV at a frequency of 100 kHz. It is seen that there are no other major harmonics present.

The spectral output of the 20 V signal generator is shown in figure 12. It is clear that there are no other major harmonics present other than the set frequency of 100 kHz. The next highest frequency is 10^5 times smaller in amplitude.